Phase transformation and electrochemical charge storage properties of vanadium oxide/carbon composite electrodes synthesized via integration with dopamine

*Ryan Andris, Timofey Averianov, Ekaterina Pomerantseva**

Department of Materials Science and Engineering, Drexel University, Philadelphia, PA 19104, USA

* Corresponding Author: ep423@drexel.edu

Keywords: *sol-gel and hydrothermal synthesis; vanadium oxides; dopamine carbonization; composites; Li-ion batteries*

Abstract

Chemically preintercalated dopamine (DOPA) molecules were used as both reducing agent and carbon precursor to prepare δ-$V_2O_5{\cdot}nH_2O$/C, $H_2V_3O_8$/C, VO_2(B)/C and V_2O_3/C nanocomposites via hydrothermal treatment or hydrothermal treatment followed by annealing under Ar flow. We found that the phase composition and morphology of the produced composites are influenced by the DOPA:V_2O_5 ratio used to synthesize $(DOPA)_xV_2O_5$ precursors through DOPA diffusion into the interlayer region of δ-$V_2O_5{\cdot}nH_2O$ framework. The increase of DOPA concentration in the reaction mixture led to more pronounced reduction of vanadium and a higher fraction of carbon in the composites' structure, as evidenced by XPS and Raman spectroscopy measurements. The electrochemical charge storage properties of the synthesized nanocomposites were evaluated in Li-ion cells with non-aqueous electrolyte. δ-$V_2O_5{\cdot}nH_2O$/C, $H_2V_3O_8$/C, VO_2(B)/C, and V_2O_3/C electrodes delivered high initial capacities of 214, 252, 279, and 637 $mAh{\cdot}g^{-1}$, respectively. The insights provided by this investigation open up the possibility of creating new nanocomposite oxide/carbon electrodes for a variety of applications such as energy storage, sensing and electrochromic devices.

Graphical Abstract

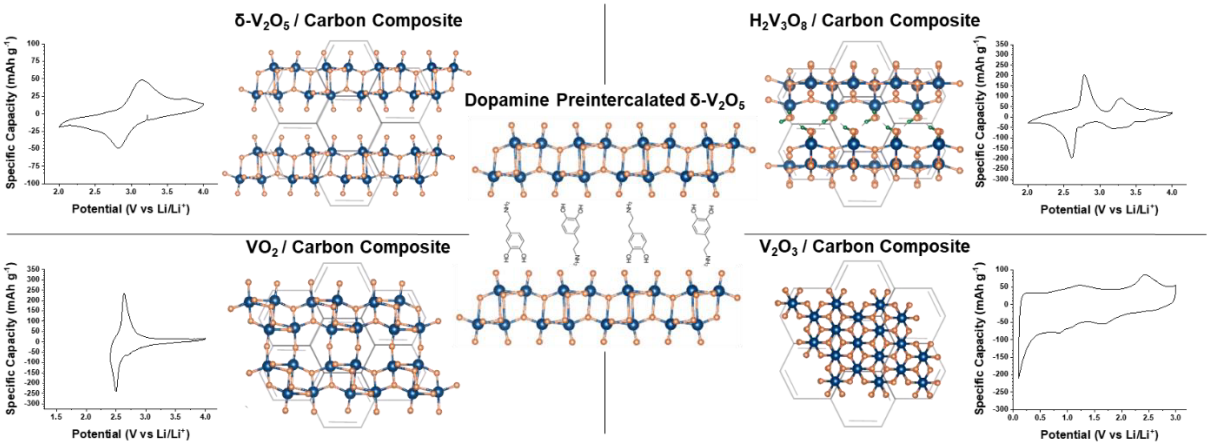

1. Introduction

Vanadium oxides have been studied extensively in electrochemical energy storage systems due to vanadium's high redox activity in reversible charge storage reactions, structural versatility, and a wide range of morphologies, stemming from different synthesis procedures and vanadium oxidation states[1-6]. Orthorhombic α-V_2O_5, monoclinic bilayered δ-$V_2O_5{\cdot}nH_2O$, $H_2V_3O_8$, VO_2(B), V_2O_3, and other vanadium oxides have been studied in Li-ion batteries as both anodes and cathodes[5, 7-10]. δ-$V_2O_5{\cdot}nH_2O$ is a promising electrode material for batteries because of its large, open, interlayer region with a *d*-spacing of approximately 11.5 Å when stabilized by water[11]. This spacing is about double that of the most common commercial cathodes and allows for the intercalation of different charge storage ions and various molecular species[1, 12-16]. In addition, the +5 oxidation state means that each vanadium atom can undergo multiple reduction steps which translates to high specific capacity[11]. The mixed-valance $H_2V_3O_8$ (i.e., V^{5+}/V^{4+}) phase maintains a high average vanadium oxidation state that corresponds to a high theoretical capacity and also results in a higher conductivity than that of δ-$V_2O_5{\cdot}nH_2O$[17]. In addition, it has a relatively open structure that allows for the intercalation of Na^+, Mg^{2+} and Zn^{2+} ions parallel to the *bc* plane[9, 18]. The VO_2(B) polymorph also has a layered structure, and it has shown reversible insertion and deinsertion of Li^+ ions[3, 19]. However, it is a metastable phase that can be oxidized in air[17]. Each of these materials has an average vanadium oxidation state of +4 to +5 that corresponds to high operating voltages in the cathodic potential window[13]. In comparison, V_2O_3 is a promising anode material because it has a theoretical capacity of 1070 $mAh{\cdot}g^{-1}$, higher than commercialized graphite, and a low discharge potential in the anodic potential window[20, 21]. However, transition metal oxides can suffer from poor capacity retention and slow charge transport kinetics due to low electronic conductivity[22, 23]. Therefore, there has been considerable research to improve their rate performance and electrochemical stability by developing transition metal oxide/carbon composites[24-30].

One synthesis strategy to form the composites is growing metal oxides on pre-existing carbon surfaces. For example, carbon nanotubes and graphene nanoplatelets were introduced into a vanadium oxide chemical preintercalation synthesis where δ-$Li_xV_2O_5{\cdot}nH_2O$ grew on the carbon surfaces during sol-gel process and aging[24]. Similarly, a different study used a combination of hydrothermal treatment and high temperature annealing to grow α-V_2O_5, VO_2(B), and V_2O_3 on reduced graphene oxide(rGO)[26]. Finally, a $H_2V_3O_8$/rGO composite was formed by hydrothermally

treating a mixture of GO and δ-$V_2O_5 \cdot nH_2O$ where the GO acts as a conducting, reducing, and structuring agent[31]. A second composite synthesis strategy involves growing or crystallizing a metal oxide phase while simultaneously carbonizing a conductive carbon precursor (e.g., glucose). For instance, a 3D hierarchical porous V_2O_3/C composite was formed by first hydrothermally treating α-V_2O_5 with glucose to form a VO_2(B)/C composite before a final annealing step produced the V_2O_3/C structure[32]. A more straightforward approach simply mixed glucose and V_2O_3 powder before hydrothermal treatment and high-temperature annealing to form a V_2O_3/C composite[27]. Different concentrations of glucose and α-V_2O_5 were also used in combination with hydrothermal treatment to systematically synthesize $H_2V_3O_8$ and VO_2 phases with different morphologies dependent on the initial glucose concentration[33]. In summary, all previously published reports demonstrated efficient formation of vanadium oxide/carbon composites that were electrochemically active in charge storage reactions. However, they did not investigate how to regulate the concentration of small organic molecules in the interlayer region of oxides, and in turn, control the final vanadium oxide phase composition.

Dopamine (DOPA) hydrochloride is a widely used carbon precursor because it can adhere to a wide range of organic and inorganic surfaces, and it has the ability to efficiently polymerize and carbonize during heat treatment processes. Yet it has only been to a limited extent studied in a vanadium oxide system[34]. DOPA is also highly soluble in water which makes it an attractive carbon precursor to incorporate into an aqueous-based synthesis approach. For example, the chemical preintercalation method consists of an aqueous sol-gel process, extended aging, and hydrothermal treatment that leads to incorporation of charged species between metal oxide layers[1, 35]. In a previous study a layered δ-$C_xV_2O_5 \cdot nH_2O$ heterostructure was formed by preintercalating DOPA molecules between vanadium oxide bilayers (in a DOPA:V_2O_5 = 1:5 molar ratio) followed by carbonization during hydrothermal treatment[36]. One drawback of this method is that only a small amount of carbon could be detected after hydrothermal treatment. However, it was shown that when a higher concentration of DOPA was used in a chemical preintercalation synthesis with molybdenum oxide (e.g., in a DOPA:Mo = 1:1 molar ratio), hydrothermal treatment and annealing led to molybdenum reduction and the formation of hollow carbon spheres coated with MoO_2 nanoplatelets[37]. MoO_2 is an anodic material, and to use the above synthesis approach for cathodes,

the synthesis requires fine adjustments to the dopamine to transition metal oxide ratio. This initial parameter can control the final oxidation state of the transition metal and structure of the oxide.

Here, DOPA was used to controllably reduce δ-$V_2O_5{\cdot}nH_2O$ with its open layered structure into diverse, more crystallographically dense vanadium oxides (**Figure 1**). Raman spectroscopy measurements confirmed that the dopamine was carbonized during both hydrothermal treatment and high temperature annealing of the dopamine preintercalated bilayered vanadium oxide precursor, leading to the formation of vanadium oxide/carbon composites. We show that each of the synthesized composites is electrochemically active as an electrode in a Li-ion energy storage system. The *in-situ* carbon formation can benefit electrochemical performance of the vanadium oxide electrodes. By exploiting the ability of DOPA molecules to simultaneously act as a reducing agent and carbon precursor, we reveal experimental parameters enabling control of the vanadium oxide phase composition in the structure of oxide/carbon composites. This study opens a pathway for the synthesis of multifunctional materials required by a broad range of applications, such as energy storage, sensing and electrochromics.

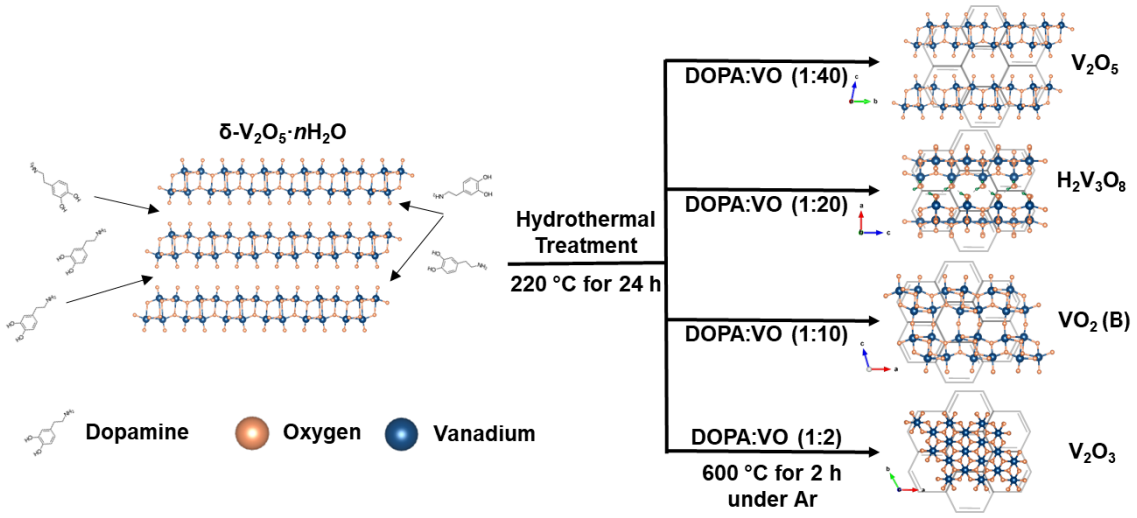

Figure 1. Schematic illustration of the multi-step synthesis process developed in this work. The process begins with the chemical preintercalation of DOPA molecules between the bilayers of δ-$V_2O_5{\cdot}nH_2O$ xerogel, followed by hydrothermal treatment and annealing processes leading to the formation of versatile vanadium oxide structures in the form of oxide/carbon composites.

2. Experimental Methods

Materials Synthesis

Bilayered δ-$V_2O_5 \cdot nH_2O$ was synthesized using a common sol-gel synthesis method[38]. Briefly, crystalline α-V_2O_5 (Acros Organics) was slowly added to a 15 wt% hydrogen peroxide solution (Fisher Scientific), and a red sol formed and precipitated after several hours. The precipitate was aged overnight, poured on a glass substrate, and dried until a xerogel formed so that only crystal-bound structural water remained. Chemical preintercalation of DOPA molecules was achieved via diffusion into the interlayer region of the pre-formed bilayered vanadium oxide structure. The xerogel flakes were added to a DOPA solution (Alfa Aesar) in the concentrations shown in **Table 1**. The flakes interacted with the solution for one day to form a hybrid precursor. Next, the flakes were filtered, dried at 105 °C in air overnight, and ground to a powder. For carbonization, the powders were hydrothermally treated in 23 mL Teflon-lined auctoclaves (Parr Instruments) with 15 mL of water at 220 °C for 24 h. To further understand the DOPA and vanadium oxide system, and for additional carbonization, some hydrothermally treated samples were separately freeze-dried (0.001 mbar , −84 °C Freezone, Labconco) and annealed at 600 °C for 2 hours under Ar flow (Thermcraft Protégé tube furnace). **Table 1** summarizes the initial DOPA:vanadium oxide (DOPA:V_2O_5) ratios and the nomenclature used for each stage of the synthesis process. The materials chosen for further study are shown in a bold font. Lastly, carbonized DOPA (C-DOPA) was synthesized to act as a reference material. First, DOPA was stirred in a Tris buffer solution for 24 hours, and the product was filtered, dried at 105 °C in air overnight, and ground to a powder. The powder was treated at 600 °C for 2 hours in an argon atmosphere to form C-DOPA.

Table 1. Summary table of DOPA:V_2O_5 ratios, the naming conventions for samples at each stage of the synthesis process.

Molar Ratio (DOPA:VO)	1:40	1to20	1to10	1to2
Hybrid Precursor	$(DOPA)_xV_2O_5$-1:40	$(DOPA)_xV_2O_5$-1:20	$(DOPA)_xV_2O_5$-1:10	$(DOPA)_xV_2O_5$-1:2
Hydrothermally Treated Composites	**HT-$(DOPA)_xV_2O_5$-1:40 → δ-$V_2O_5 \cdot nH_2O$/C**	**HT-$(DOPA)_xV_2O_5$-1:20 → $H_2V_3O_8$/C**	**HT-$(DOPA)_xV_2O_5$-1:10 → VO_2(B)/C**	HT-$(DOPA)_xV_2O_5$-1:2 → amV_2O_3/C
Annealed and Hydrothermally Treated Composites	N/A	An-HT-$(DOPA)_xV_2O_5$-1:20 → α-V_2O_5/C and V_6O_{13}/C	An-HT-$(DOPA)_xV_2O_5$-1:10 → VO_2(R)/C and V_6O_{13}/C	**An-HT-$(DOPA)_xV_2O_5$-1:2 → V_2O_3/C**

Materials Characterization

The phase composition of the materials during each stage of the synthesis process was determined using a Rigaku benchtop powder X-ray diffractometer (XRD) with Cu K_α (λ = 1.54 Å) radiation. XRD patterns were collected using a step size of 0.02° and step speed of 0.7° 2θ·min^{-1}. The morphology of the particles was captured using a Zeiss Supra 50VP scanning electron microscopy (SEM) instrument equipped with Schottky field emission and Everhart-Thornley in-lens secondary electron detectors. SEM images were acquired using a beam accelerating voltage of 5 kV. Additionally, samples were sputter coated with a thin ~5 nm layer of Pt/Pd to prevent surface charging and improve image quality. Water and DOPA contents were evaluated using thermogravimetric analysis (TGA) under ambient air flow using a TA Instruments Q50 by evaluating weight loss from room temperature to 1000 °C using a heating rate of 10 °C·min^{-1}. Fourier-transform infrared (FTIR) spectra were collected from 500 to 4000 cm^{-1} using a Nicolet 6700 FTIR spectrometer. Raman spectra were collected from 100 to 2000 cm^{-1}, using a Renishaw inVia Raman microscope equipped with a 514 nm Ar-ion laser. X-ray photoelectron spectroscopy (XPS) measurements were recorded on a Physical Electronics VersaProbe 5000 using a monochromatic Al Kα source and charge compensation. The high-resolution V 2p spectra were taken at a pass energy of 23.5 eV with a step size of 0.05 eV. Peak fitting and data analysis were carried out using CasaXPS software. A Shirley background was used for V 2p spectra quantification.

Electrode and Cell Fabrication

Electrodes were fabricated by first grinding the active material (70 wt%) and acetylene black (20 wt%) in a mortar with pestle. Next, this mixture was dispersed in poly(vinylidene fluoride) (10 wt%) and N-methyl-2-pyrrolidone (NMP) to form a viscous slurry using a Flacktek SpeedMixer. The prepared slurry was cast on aluminum foil and dried in a glovebox overnight before being placed in an oven at 105 °C for 12 h. 10 mm electrode disks were cut from the dried films. Coin cells were assembled in an argon filled glovebox.

Electrochemical Testing

All electrochemical data was collected using 2032 type coin cells. Metallic Li (Alfa Aesar) served as both the counter and reference electrodes, a polypropylene and polyethylene membrane (2325, Celgard USA) served as the separator, and the electrolyte was 1 M $LiPF_6$ dissolved in a 1:1

(v:v) mixture of ethylene carbonate (EC) and diethyl carbonate (DEC) (Gotion LP40). Cyclic voltammograms (CVs) were collected using a BioLogic VP3 potentiostat at a sweep rate of 0.1 $mV \cdot s^{-1}$. Galvanostatic cycling experiments were run at a 20 $mA \cdot g^{-1}$ charge/discharge rate on an Arbin battery testing station. Lastly, rate capability experiments were conducted for 10 cycles each at specific currents of 20 $mA \cdot g^{-1}$, 50 $mA \cdot g^{-1}$, 100 $mA \cdot g^{-1}$, 200 $mA \cdot g^{-1}$, and 20 $mA \cdot g^{-1}$.

3. Results and Discussion

An overview of the synthesis procedure is shown schematically in **Figure 1**. During the interaction between DOPA and the open layered structure of δ-$V_2O_5 \cdot nH_2O$, the DOPA concentration gradient and electrostatic forces helped the positively charged DOPA molecules diffuse between the negatively charged vanadium oxide bilayers to occupy the interlayer region. This diffusion strategy allows for more DOPA molecules to enter the interlayer region of δ-$V_2O_5 \cdot nH_2O$ as compared to the chemical preintercalation synthesis approach[36]. This effect is clearly indicated by the XRD patterns, TGA curves, and FTIR spectra shown in **Figure 2** and **Figure S1** in the **Supporting Information**.

The XRD pattern of each hybrid precursor prior to hydrothermal treatment exhibits characteristic (00*l*) peaks typical for layered structures. The (001) peak is located between 5 and 10° 2θ and corresponds to the *d*-spacing, or the distance between the centers of the vanadium oxide bilayers (**Figure 2a**). The *d*-spacing for each sample was calculated from the position of the peak using Bragg's law, and it is shown next to each (001) peak in **Figure 2a**. The *d*-spacing of the bilayered V_2O_5 depends on both the nature and the amount of the preintercalated species (i.e., water and DOPA molecules). There is a general trend towards expanded interlayer spacings with increasing DOPA:V_2O_5 ratios, except for the $(DOPA)_xV_2O_5$-1:10 sample. A possible explanation for this anomaly is that at the DOPA:V_2O_5 ratio of 1:10, enough DOPA is preintercalated so that the positive charges draw the bilayers together, but not enough to pack the interlayer region so that the axis along the amine group through the aromatic ring of the DOPA molecule is oriented more perpendicular to the vanadium oxide bilayers. In comparison, this axis is likely more parallel to the bilayers in the $(DOPA)_xV_2O_5$-1:40 sample. Most importantly, the primary (001) peak in each sample, and its lower intensity reflections, are in agreement with previous structural analysis of the monoclinic δ-$V_2O_5 \cdot nH_2O$ phase comprised of bilayered stacks of distorted edge sharing VO_6

octahedra[11].

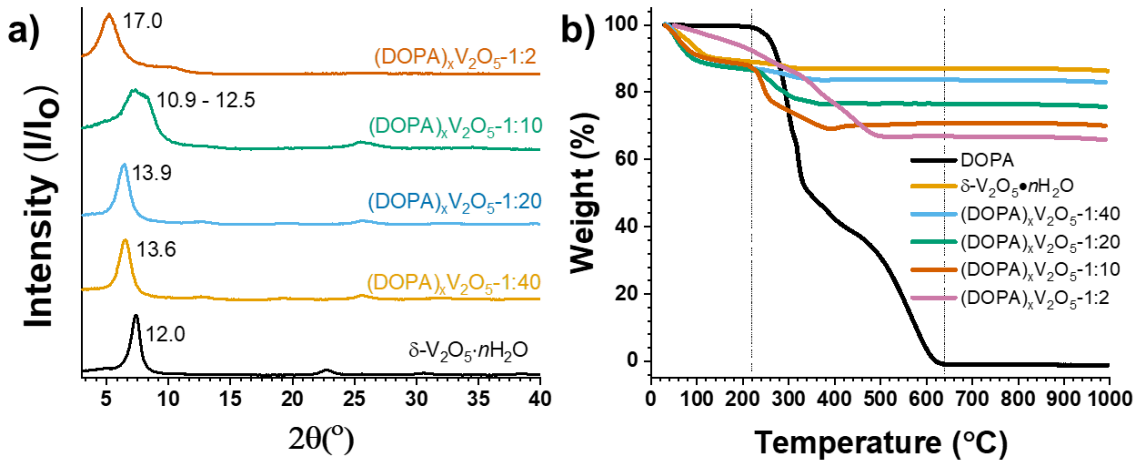

Figure 2. (a) XRD patterns and (b) TGA weight loss curves of the hybrid $(DOPA)_xV_2O_5$ precursors synthesized using different DOPA:V_2O_5 ratios.

The TGA weight loss curves of the hybrid $(DOPA)_xV_2O_5$ precursors in **Figure 2b** exhibit three primary weight loss regions. Any weight loss that occurs before approximately 100 °C and between 100 °C and 220 °C can be attributed to physiosorbed and structural water, respectively. Notably, the DOPA hydrochloride reference does not display any weight loss before 220 °C. Therefore, to estimate the DOPA content present between the bilayers, the weight loss that occurs above 220 °C for the pure δ-$V_2O_5 \cdot nH_2O$ was subtracted from the weight loss for each of the DOPA intercalated materials in the same region. The weight loss from DOPA was estimated to be 1.6 %, 7.9 %, 10 %, and 23 % for the 40:1, 20:1, 10:1, and 2:1 molar ratios, respectively. This result agrees with the idea that DOPA content increases with increasing DOPA:V_2O_5 ratios. This approach does not allow us to accurately determine the precursors' formula because DOPA molecules and water compete for the space in the interlayer region and subtracting the water weight of the pristine bilayered vanadium oxide could underestimate the DOPA content in the hybrid samples. However, this method allows to comparably evaluate the interlayer DOPA content in the $(DOPA)_xV_2O_5$ precursors.

To further confirm the presence of DOPA molecules in the interlayer region of the bilayered vanadium precursors, the FTIR spectra of δ-$V_2O_5 \cdot nH_2O$ and the $(DOPA)_xV_2O_5 \cdot nH_2O$ preintercalated materials were analyzed (**Figure S1** in **Supporting Information**). The δ-$V_2O_5 \cdot nH_2O$ phases are characterized by three absorption bands centered at approximately 990,

730, and 500 cm^{-1} that correspond to V-O stretching, asymmetric V-O-V stretching, and symmetric V-O-V stretching, respectively[39]. In addition, there is a peak at about 1610 cm^{-1} that likely belongs to interstitial water vibrations[40]. As the DOPA content increases, the region between 1100 and 1610 cm^{-1} broadens and decreases in transmittance which can be the result of an increase in organic content from DOPA between the vanadium bilayers[16, 41]. The region around 3400 cm^{-1} is another area that typically captures vibrations of organic molecules and interstitial water[16, 41, 42]. It is possible that the $(DOPA)_xV_2O_5 \cdot nH_2O$ spectra in **Figure S1** show a broader band in this region; however, it is challenging to make definitive conclusions. The lack of pronounced differences in this area could be attributed to the reflection-type FTIR utilized in this study compared to transmission-type FTIR seen commonly in literature.

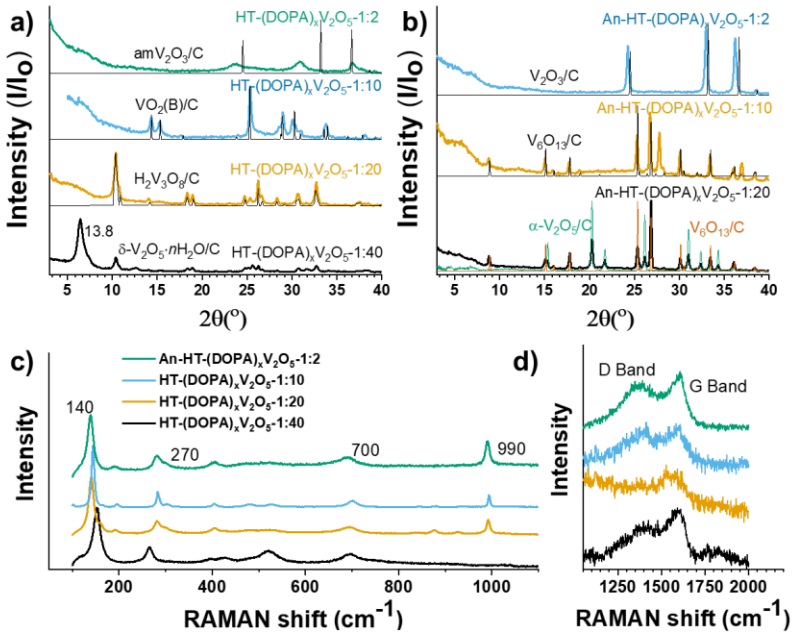

Figure 3. (a, b) XRD patterns of the (a) HT-$(DOPA)_xV_2O_5$ samples (i.e., after hydrothermal treatment) and (b) An-HT-$(DOPA)_xV_2O_5$ samples (i.e., after hydrothermal treatment and annealing at 600°C under Ar flow), and (c, d) Raman spectra of the final single-phase materials (i.e., HT-$(DOPA)_xV_2O_5$-1:40, HT-$(DOPA)_xV_2O_5$-1:20, HT-$(DOPA)_xV_2O_5$-1:10, and An-HT-$(DOPA)_xV_2O_5$1:2 which are the δ-$V_2O_5 \cdot nH_2O$/C, $H_2V_3O_8$/C, VO_2(B)/C, and V_2O_3/C phases, respectively). Regions corresponding to the vanadium oxide framework and carbon are shown in (c) and (d), respectively.

The XRD patterns in **Figure 3a** and **3b** show the phase transformations that occur through heat treatment processing and provide further evidence that increasing amounts of DOPA preintercalated into the bilayered vanadium phase. The XRD peaks of the reference phases are overlain in black lines[3, 43, 44]. The HT-$(DOPA)_xV_2O_5$-1:40 material still exhibits the (00*l*)

reflections, indicative of the bilayered phase in which vanadium has a 5+ oxidation state, in addition to peaks belonging to $H_2V_3O_8$. This mixed valence V^{5+} / V^{4+} impurity implies that DOPA is capable of measurably reducing vanadium even in small concentrations. The $(DOPA)_xV_2O_5$-1:20 sample underwent a full transformation to $H_2V_3O_8$ with strong peaks characteristic of the orthorhombic phase with high crystallinity. Further, the $(DOPA)_xV_2O_5$-1:10 material resulted in a pure metastable VO_2(B) phase with diffraction peaks indexed to its monoclinic unit cell. Finally, the HT-$(DOPA)_xV_2O_5$-1:2 sample seems like it may be an amorphous phase with peaks that roughly correspond to V_2O_3, but with broad and rounded peaks that indicate low crystallinity. We called this sample amV_2O_3. Therefore, samples prepared with higher DOPA:V_2O_5 ratios resulted in a higher degree of vanadium reduction after hydrothermal treatment. This phenomenon could be due to an increase of hydroxyl groups available for vanadium reduction[33, 45]. In addition, there could also be a complementary reducing effect from the DOPA derived carbon present in each sample[32]. The phase transformations to vanadium oxide phases with increasingly lower vanadium oxidation states can only be the result of interactions between the δ-$V_2O_5{\cdot}nH_2O$ bilayers and increasing DOPA content.

In an attempt to fully crystallize the amV_2O_3 phase and further carbonize the organic precursor, the HT-$(DOPA)_xV_2O_5$-1:2, HT-$(DOPA)_xV_2O_5$-1:10, and HT-$(DOPA)_xV_2O_5$-1:20 materials were annealed at 600 °C under Ar flow[32, 37, 46]. This heat treatment fully crystallized the HT-$(DOPA)_xV_2O_5$-1:2 sample into rhombohedral V_2O_3 as shown in **Figure 3b**. In contrast, the HT-$(DOPA)_xV_2O_5$-1:10 and HT-$(DOPA)_xV_2O_5$-1:20 samples formed new materials. The metastable VO_2(B) underwent a phase transformation to V_6O_{13} as can be seen in the overlain reference. Further, the peaks that can't be indexed to V_6O_{13} (e.g., the peaks at 27.8 and 37.0 2Θ°) correspond to rutile-like vanadium oxide known as VO_2(R). This phase transformation is well documented above 300 °C[47]. Similarly, the crystallographic water in the HT-$(DOPA)_xV_2O_5$-1:20 material (i.e., $H_2V_3O_8$) is removed at high temperatures, which induced a phase transformation to both V_6O_{13} and α-V_2O_5. The water likely played a role in the partial oxidation to the V^{5+} present in V_2O_5. Annealing the HT-$(DOPA)_xV_2O_5$-1:2 sample at 600 °C resulted in a fully crystalline V_2O_3 phase . However, this treatment also caused unwanted phase changes in the VO_2(B) and $H_2V_3O_8$ structures that were less stable at high temperatures.

The single-phase materials, V_2O_3/C , VO_2(B)/C, and $H_2V_3O_8$/C, along with the sample with the highest average vanadium oxidation state, δ-$V_2O_5 \cdot nH_2O$/C, were chosen for Raman characterization (**Figure 3c**). The Raman spectra from 100 - 1100 cm^{-1} contain bands associated with the fingerprints of vanadium oxide frameworks, where the spectral bands are characteristic of these materials[36, 47, 48]. The primary region of interest is from 1200 – 1700 cm^{-1} where two broad bands can be seen at approximately 1370 and 1580 cm^{-1} that can be assigned to the D and G bands of carbon[49, 50]. The presence of these peaks provides strong evidence that DOPA molecules both reduce vanadium and carbonize during hydrothermal treatment. To our knowledge, this result has not been previously demonstrated using dopamine in a bilayered vanadium oxide system. It is in agreement with previous studies, and it could be an efficient method to synthesize material composites with inherent carbon content and tight oxide/carbon contact that could be beneficial for electrochemical applications[36, 51]. However, the prominent D band indicates that the formed carbon is defect-rich and is likely amorphous in nature. The carbon present in the synthesized materials, as evidenced by carbon D and G bands in the Raman spectra, is in agreement with the TGA results that showed the presence of DOPA within the vanadium oxide bilayers prior to heat treatment.

Figure 4 shows SEM images of various $(DOPA)_xV_2O_5$, HT-$(DOPA)_xV_2O_5$, and An-HT-$(DOPA)_xV_2O_5$ powders. **Figure 4a** demonstrates the typical layered morphology of the $(DOPA)_xV_2O_5$ hybrid precursors prior to any heat treatment processing. Each $(DOPA)_xV_2O_5$ sample is comprised of 2D lamellar sheets stacked to form several microns thick agglomerates, regardless of the amount of DOPA preintercalated between the layers. After hydrothermal treatment, the sample morphologies exhibit a general trend towards higher dimensions and smaller aspect ratios with increasing DOPA:V_2O_5 ratios. For example, the HT-$(DOPA)_xV_2O_5$-1:40 material (i.e., δ-$V_2O_5 \cdot nH_2O$/C) maintained the 2D sheet-like morphology, albeit it seems as though some delamination occurred during the hydrothermal process to form more crystalline looking sheets with dimensions tens to hundreds of μms across (**Figure 4b**). Next, increasing the DOPA:V_2O_5 ratio to 1:20 formed $H_2V_3O_8$/C after hydrothermal treatment and resulted in the full exfoliation and splitting of the 2D sheets into elongated nanowires (**Figure 4c**). These nanowires are approximately 0.1 μm wide and tens to hundreds of microns long. This reducing-exfoliating-splitting mechanism has been discussed in previous works that synthesized the $H_2V_3O_8$ phase[33, 52]. Further, the $(DOPA)_xV_2O_5$-1:10 material resulted in VO_2(B)/C nanobelts 0.1 to 0.3 μm wide and

approximately 5 μm long (**Figure 4d**). Finally, the $(DOPA)_xV_2O_5$-1:2 sample formed 3D spheroids with dimensions of approximately 0.5 μm (**Figure 4e**). DOPA commonly forms spheres in both its polymerized and carbonized state, and it is possible that these spheroids are DOPA spheres coated in V_2O_3 material[37, 50]. This amV_2O_3/C phase was then fully crystallized after high temperature annealing accompanied by the formation of more distinctly defined V_2O_3 crystallites as shown in **Figure 4f**.

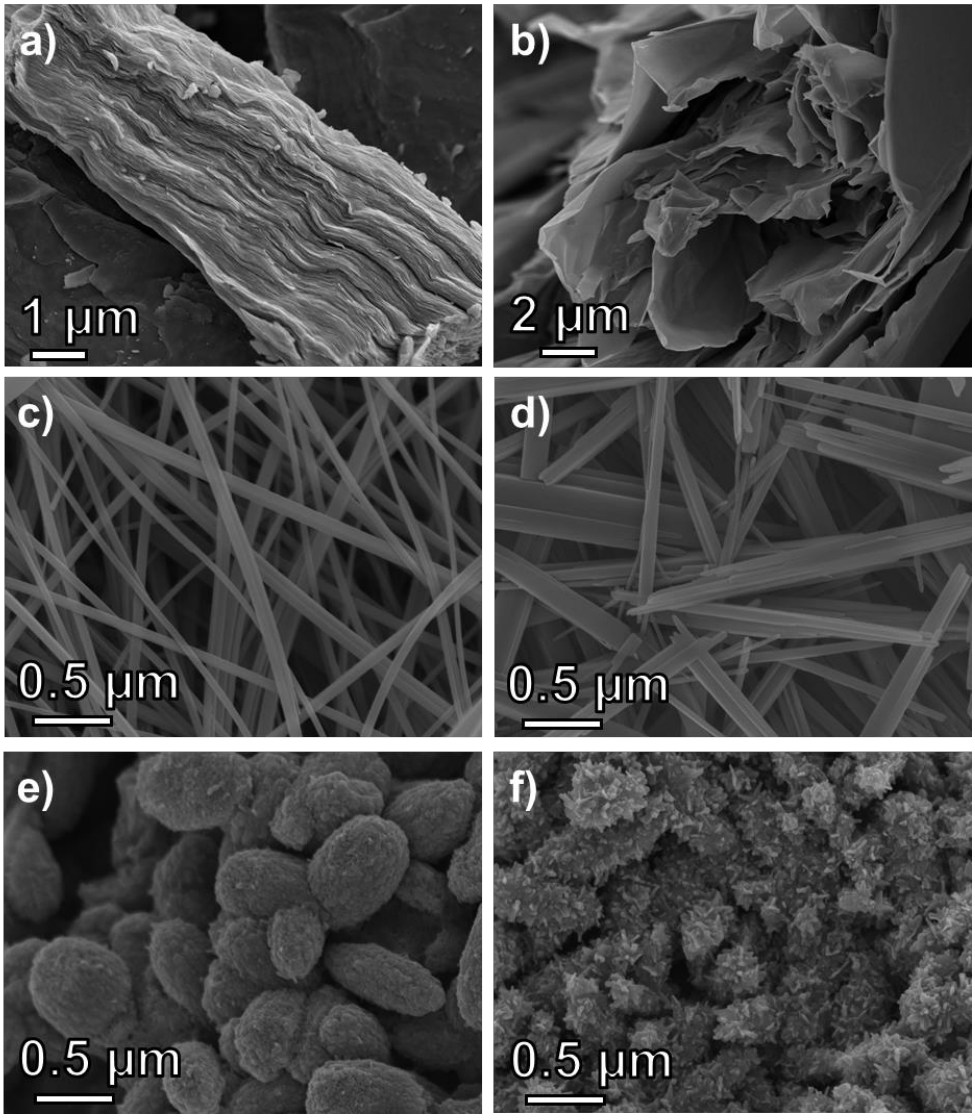

Figure 4. SEM images of the (a) typical layered structure of $(DOPA)_xV_2O_5$ hybrid precursors prior to hydrothermal treatment, (b) δ-$V_2O_5{\cdot}nH_2O$/C, (c) $H_2V_3O_8$/C, (d) VO_2(B)/C, (e) amV_2O_3/C after hydrothermal treatment, and (f) the final crystalline V_2O_3/C phase after hydrothermal treatment and annealing.

XPS measurements were performed to gain insight into how different DOPA:V_2O_5 ratios affected the oxidation state of vanadium at each stage of the synthesis process. The spectra are displayed in **Figure 5** and the estimated fractions of V^{5+}, V^{4+}, and V^{3+} ions in each material are shown in **Table 2**. Before hydrothermal treatment, vanadium maintains a 5+ oxidation state in the samples with the lowest DOPA content (i.e., $(DOPA)_xV_2O_5$-1:40 and $(DOPA)_xV_2O_5$-1:20). In contrast, the $(DOPA)_xV_2O_5$-1:10 and $(DOPA)_xV_2O_5$-1:2 samples did undergo some vanadium reduction during the preintercalation process, marked by the V^{4+} component in their spectra. This result could indicate interactions between the vanadium in the bilayers and the DOPA molecules that result in vanadium reduction and the initialization of DOPA polymerization within the interlayer space, a similar phenomenon to that seen in previous work[53].

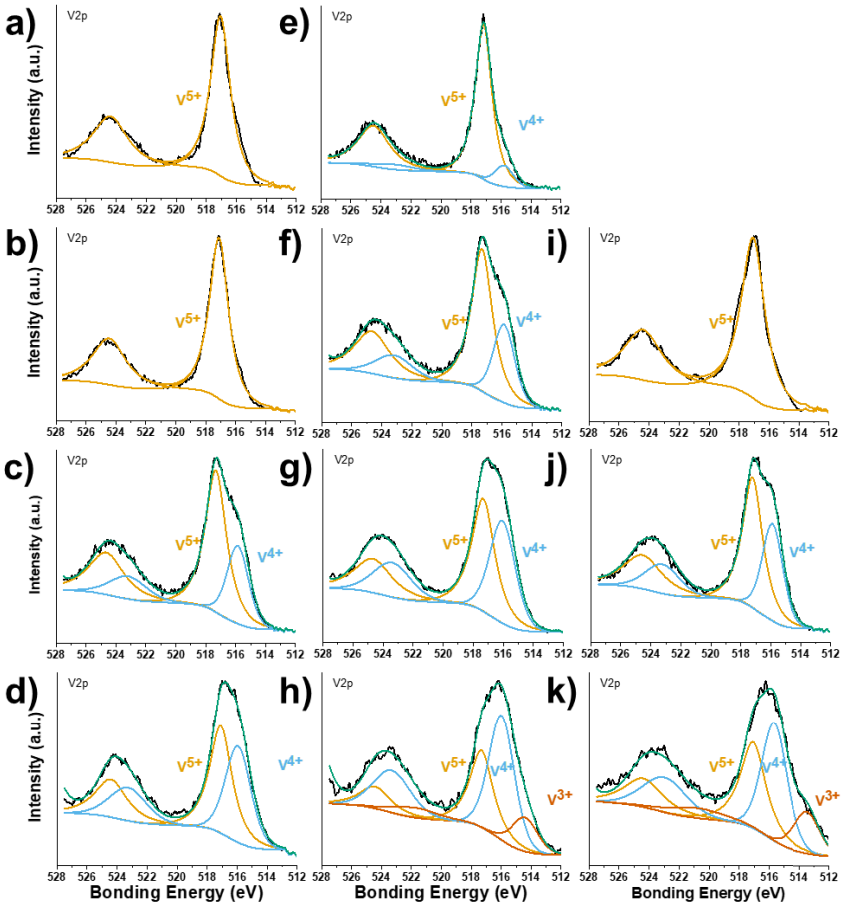

Figure 5. XPS spectra of the V2p region for (a-d) $(DOPA)_xV_2O_5$ synthesized with DOPA:V_2O_5 (a) 1:40, (b) 1:20, (c) 1:10, and (d) 1:2 precursor ratios before hydrothermal treatment; (e) δ-$V_2O_5{\cdot}nH_2O$/C, (f) $H_2V_3O_8$/C, (g) VO_2(B)/C, and (h) amV_2O_3/C after hydrothermal treatment; and the multiphase (i) 1:20, (j) multiphase 1:10, and (k) crystalline V_2O_3/C after high temperature annealing.

Table 2. Summary table of XPS data analysis reporting fractions of V^{5+}, V^{4+}, and V^{3+} ions in each material.

Sample	V^{5+} Atomic %	V^{4+} Atomic %	V^{3+} Atomic %
$(DOPA)_xV_2O_5$-1:40	100	0	0
$(DOPA)_xV_2O_5$-1:20	100	0	0
$(DOPA)_xV_2O_5$-1:10	83.4	16.6	0
$(DOPA)_xV_2O_5$-1:2	53.2	46.8	0
HT-$(DOPA)_xV_2O_5$-1:40	88.4	11.6	0
HT-$(DOPA)_xV_2O_5$-1:20	67.4	32.6	0
HT-$(DOPA)_xV_2O_5$-1:10	53.3	46.7	0
HT-$(DOPA)_xV_2O_5$-1:2	30.5	54.3	15.2
An-HT-$(DOPA)_xV_2O_5$-1:20	100	0	0
An-HT-$(DOPA)_xV_2O_5$-1:10	60.4	39.6	0
An-HT-$(DOPA)_xV_2O_5$-1:2	38.3	45.5	16.2

The XPS spectra of the HT-$(DOPA)_xV_2O_5$ samples demonstrate a clear trend where samples prepared with more DOPA exhibit a higher degree of vanadium reduction. The hydrothermal treatment process simultaneously polymerizes and carbonizes the DOPA molecules, thereby continuing the vanadium reduction process, as well as initiating the exfoliation and splitting of the δ-V_2O_5 nanosheets. This result is most clearly seen in the V^{5+} component (i.e., the orange curves) decreasing from roughly 88% in the HT-$(DOPA)_xV_2O_5$-1:40 sample to approximately 31% in the HT-$(DOPA)_xV_2O_5$-1:2 sample. This sample also shows a V^{3+} component which is appropriate given the stoichiometry of V_2O_3. Moreover, there is evidence of oxidation occurring during annealing at 600 °C in an inert atmosphere, similarly to the dopamine preintercalated molybdenum oxide system[37]. In particular, the XPS measurement did not find any V^{4+} component in the An-HT-$(DOPA)_xV_2O_5$-1:20 material. As discussed previously, this result is likely explained by the water and hydroxyl groups content in the sample. Similarly, the partial oxidation of VO_2 and V_2O_3 can likely be explained by trace amounts of water remaining in the samples after drying.

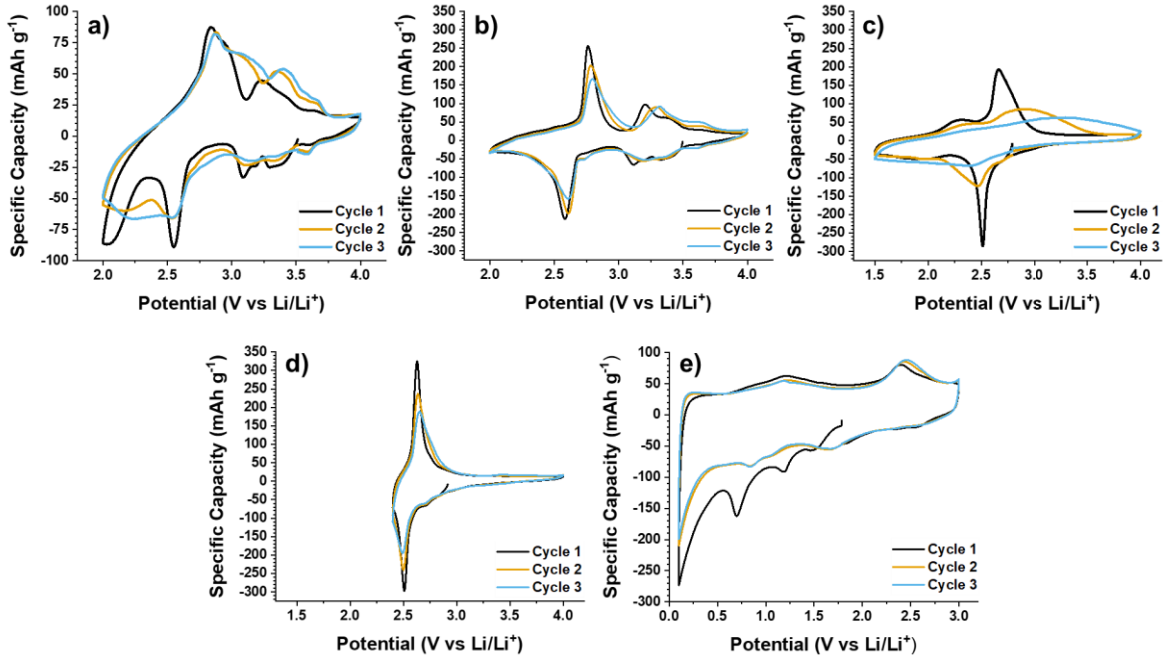

Figure 6. 1st, 2nd and 3rd cycle CV curves of the Li-ion cells containing (a) δ-$V_2O_5{\cdot}nH_2O$/C, (b) $H_2V_3O_8$/C, (c, d) VO_2(B)/C, and (e) V_2O_3/C electrodes cycled at a sweep rate of 0.1 $mV{\cdot}s^{-1}$.

The electrochemical performance of δ-$V_2O_5{\cdot}nH_2O$/C, $H_2V_3O_8$/C, VO_2(B)/C, V_2O_3/C electrodes was evaluated in Li-ion half-cells. The CV curves for each respective material are shown in **Figure 6**. The 1st cycle CV curve of the cell containing a δ-$V_2O_5{\cdot}nH_2O$/C electrode (**Figure 6a**) exhibits two broad cathodic peaks between 3.0 and 3.5 V, a sharp peak at 2.5 V, and an additional discharge region below 2.3 V. The corresponding anodic peaks are at approximately 2.8 and 3.2 V. Upon cycling, these regions broaden, but they remain stable. These peaks are likely the result of both diffusion limited Li^+ intercalation between the δ-V_2O_5 layers and surface redox charge storage that is responsible for the broad nature of the peaks. The initial capacity is approximately 214 $mAh{\cdot}g^{-1}$. A similar material was synthesized in our research group using a chemical preintercalation approach and further electrochemical discussion can be found in this publication[36]. The $H_2V_3O_8$/C phase (**Figure 6b**) exhibits sharp and reversible cathodic and anodic peaks at 2.6 and 2.8 V, respectively, and a high capacity of 250 $mAh{\cdot}g^{-1}$, an improvement over pristine $H_2V_3O_8$ electrode capacities shown in previous reports[2, 9]. This peak shape corresponds to more traditional battery-like behavior where charge storage is dominated by diffusion-limited redox processes. Similarly, the VO_2(B)/C material (**Figure 6c** and **6d**) shows peaks at approximately 2.5 and 2.6 V in the CV curve. This phase was cycled in two potential windows of 1.5 – 4.0 V and 2.4 – 4.0 V vs. Li/Li^+. Narrowing the potential window led to far better

electrochemical stability. This result is likely due to the extended discharging step to 1.5 V vs. Li/Li^+ in the larger window that could lead to structure degradation. Moreover, this degradation seems to lead to less diffusion-limited charge storage. One drawback of limiting the potential window is it predictably restricts the initial cycling capacity. In this instance, in the larger 1.5 – 4.0 V potential window an initial capacity of 279 $mAh \cdot g^{-1}$, compared to 168 $mAh \cdot g^{-1}$ in the 2.4 – 4.0 V potential window. The capacity in the smaller window is in agreement with a VO_2(B) phase synthesized through low-temperature vacuum annealing of a δ-$V_2O_5 \cdot nH_2O$ aerogel[3]. Further, the larger window shows initial electrochemical performance similar to or better than previous work[17, 33, 54]. Lastly, V_2O_3 (**Figure 6e**) is an anode material active at much lower potential windows. The 1st cycle CV curve of the cell containing a V_2O_3/C electrode exhibits several cathodic peaks with the most prominent one appearing at 0.7 V vs. Li/Li^+ that disappears after the initial discharge. This activity is probably the result of SEI formation on the V_2O_3/C spheroids that contributes to an initial capacity of 637 $mAh \cdot g^{-1}$. The remaining cycles show predominantly surface charge storage that correlates well with the morphology of this material, and a capacity of approximately 446 $mAh \cdot g^{-1}$, an improvement over a study that synthesized V_2O_3 composites using carboxylic acids as the carbon source[5]. To evaluate the electrochemical activity of the V_2O_3 in the composite material, C-DOPA was also cycled in a Li-ion half-cell. Figure S2 (Supporting Information) shows the results of galvanostatic life cycle testing of these materials. The observed discharge/charge profiles reveal that both V_2O_3 and dopamine-derived carbon are electrochemically active in the similar potential range, making it challenging to evaluate individual contributions of the material to the overall observed capacity. However, it also appears that V_2O_3 lends stability to the nanostructure. After 75 cycles, V_2O_3/C and C-DOPA electrodes retained approximately 76% and 33% of their respective initial capacities and exhibited absolute capacities of 481 $mAh \cdot g^{-1}$ and 317 $mAh \cdot g^{-1}$, respectively.

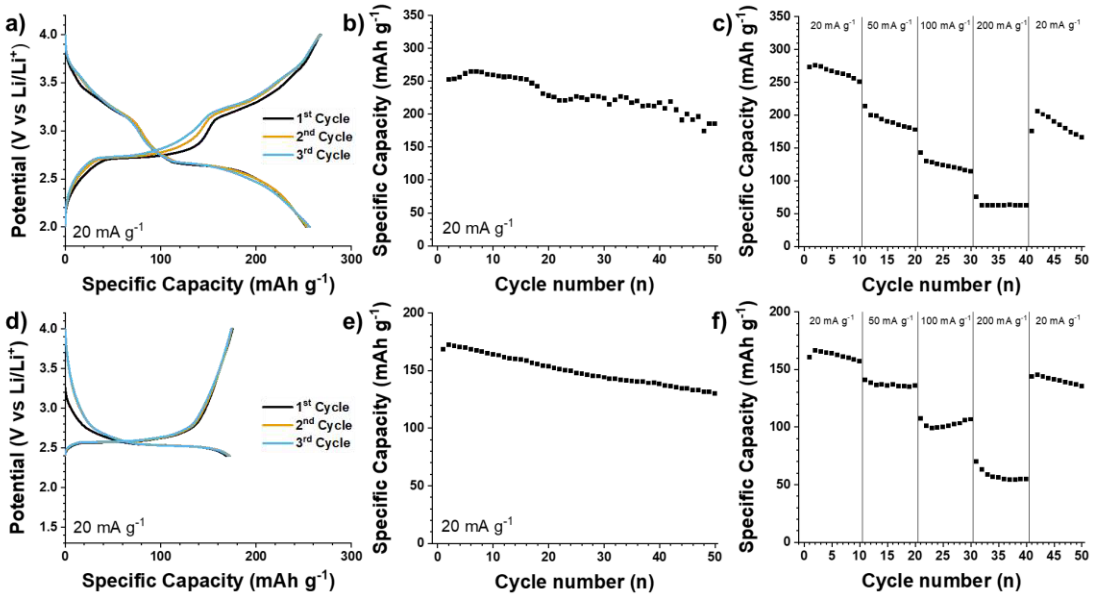

Figure 7. (a, d) Galvanostatic charge and discharge curves, (b, e) cycle life, and (c, f) rate capability data of the Li-ion cells containing (a-c) $H_2V_3O_8$/C and (d-f) VO_2(B)/C electrodes, respectively.

The CV measurements demonstrate that the $H_2V_3O_8$/C and VO_2(B)/C electrodes exhibit a promising combination of capacity and stability in the potential window corresponding to cathodic activity, and therefore they were selected to further characterize their electrochemical stability and rate capability (**Figure 7**). Their respective galvanostatic charge and discharge curves (**Figure 7a** and **7d**) display plateaus at in the same potential windows as the peaks in the CV curves, an additional confirmation that the intercalation and deintercalation of ions occurs at these potentials. The 1st cycle specific discharge capacity of 252 mAh·g^{-1} and 168 mAh·g^{-1} were demonstrated by Li-ion cells containing $H_2V_3O_8$/C and VO_2(B)/C electrodes, respectively. Galvanostatic cycling shows that $H_2V_3O_8$/C and VO_2(B)/C materials retained approximately 74% and 77% of their respective initial capacities after 50 cycles. Both materials showed better life cycle performance than a study that used glucose to synthesize both $H_2V_3O_8$ and VO_2[33]. Lastly, their rate capability was examined to assess the ability to undergo fast charging and discharging. $H_2V_3O_8$/C demonstrated a 77% specific capacity fade to about 63 mAh·g^{-1} moving from 20 mA·g^{-1} to 200 mA·g^{-1}. In comparison, VO_2(B)/C retained approximately 34% of its capacity with the same increase in specific current over 40 cycles. The capacity decay can be attributed to the structural instability of vanadium oxides caused by interactions with DOPA, dissolution of vanadium oxides in electrolyte in the course of cycling, and inefficient integration of carbon and oxide components in the composites' structure. Improved results can be obtained by utilizing organic molecule

carbon precursors other than dopamine hydrochloride. An interesting alternative is aromatic organic molecules without oxygen and hydroxyl groups in their chemical composition, such as o-phenylenediamine, currently explored by our group. The developed synthesis approach allows for the investigation of versatile organic molecules for the synthesis of oxide/carbon composite electrodes and establishing relationships between the structure/chemical composition of the employed organic molecules and electrochemical charge storage properties of the produced materials.

4. Conclusions

In summary, by setting up experimental conditions that allow DOPA molecules to diffuse into the interlayer region of bilayered vanadium oxide, followed by hydrothermal treatment or hydrothermal treatment and annealing in inert atmosphere, we prepared δ-$V_2O_5{\cdot}nH_2O$/C, $H_2V_3O_8$/C, VO_2(B)/C and V_2O_3/C composites exhibiting electrochemical activity in charge storage reactions. The developed diffusion synthesis method enabled reliable chemical intercalation of controlled amounts of DOPA that resulted in progressive reduction of the parent δ-$V_2O_5{\cdot}nH_2O$ xerogel to various electrochemically active vanadium oxide phases depending on the initial DOPA:V_2O_5 ratio. The presence of carbon in the structure of the produced materials, revealed by Raman spectroscopy measurements, warrants our finding that DOPA acted as both a reducing agent and a carbon precursor. Moreover, controlling the concentration of DOPA was shown to direct the morphologies of the synthesized materials. Interaction between the interlayer DOPA molecules and bilayered vanadium oxide framework proceeds according to a complex mechanism which requires a separate study.

δ-$V_2O_5{\cdot}nH_2O$/C, $H_2V_3O_8$/C, VO_2(B)/C and V_2O_3/C electrodes demonstrated high initial specific capacities of 214, 252, 279, and 637 $mAh{\cdot}g^{-1}$ in non-aqueous Li-ion cells, respectively. These results motivate further exploration of the developed synthesis approach with new organic molecules that can be employed as carbon precursors. In particular, this approach can use molecules that create a more stable heterointerface and limit architectural evolution that can occur during electrochemical cycling. It would also be beneficial to explore organic molecules that may limit phase transformations that can occur during hydrothermal treatment and annealing in inert atmosphere. This approach could help the δ-$V_2O_5{\cdot}nH_2O$ precursor maintain its open 2D structure while increasing conductive carbon content, and in turn, improve electrochemical performance.

Finally, this synthesis method could utilize alternative transition metal oxides to create a library of materials that can transport electrons and undergo redox reactions for potential applications in energy storage, sensing, electrocatalysis, and electrochromic devices.

Acknowledgements

This work was supported by the National Science Foundation (NSF) under Grant No. DMR-1752623. The Labconco freeze-drier was purchased using NSF funds under Grant No. DMR-1609272. The purchase of the Thermcraft Protégé tube furnace was supported by the Center for Mesoscale Transport Properties, an Energy Frontier Research Center supported by the U.S. Department of Energy, Office of Science, Basic Energy Sciences via grant #DE-SC0012673. We acknowledge Drexel's Materials Characterization Core (MCC) facility for providing access to characterization instruments and the Alvarez Research Group for providing access to their Nicolet FTIR spectrometer.

References

1. Clites, M.; Pomerantseva, E., Bilayered vanadium oxides by chemical pre-intercalation of alkali and alkali-earth ions as battery electrodes. *Energy Storage Materials* **2018,** *11*, 30-37.
2. Zhu, K.; Yan, X.; Zhang, Y.; Wang, Y.; Su, A.; Bie, X.; Zhang, D.; Du, F.; Wang, C.; Chen, G.; Wei, Y., Synthesis of $H_2V_3O_8$/Reduced Graphene Oxide Composite as a Promising Cathode Material for Lithium-Ion Batteries. *ChemPlusChem* **2014,** *79* (3), 447-453.
3. Baudrin, E.; Sudant, G.; Larcher, D.; Dunn, B.; Tarascon, J.-M., Preparation of Nanotextured VO_2[B] from Vanadium Oxide Aerogels. *Chemistry of Materials* **2006,** *18* (18), 4369-4374.
4. Corr, S. A.; Grossman, M.; Shi, Y.; Heier, K. R.; Stucky, G. D.; Seshadri, R., VO_2(B) nanorods: solvothermal preparation, electrical properties, and conversion to rutile VO_2 and V_2O_3. *Journal of Materials Chemistry* **2009,** *19* (25), 4362.
5. Zakharova, G. S.; Thauer, E.; Enyashin, A. N.; Deeg, L. F.; Zhu, Q.; Klingeler, R., V_2O_3/C composite fabricated by carboxylic acid-assisted sol–gel synthesis as anode material for lithium-ion batteries. *Journal of Sol-Gel Science and Technology* **2021,** *98* (3), 549-558.
6. Chernova, N. A.; Roppolo, M.; Dillon, A. C.; Whittingham, M. S., Layered vanadium and molybdenum oxides: batteries and electrochromics. *Journal of Materials Chemistry* **2009,** *19* (17), 2526.
7. Chuanfang; Park, S.-H.; O'Brien, S. E.; Seral-Ascaso, A.; Liang, M.; Hanlon, D.; Krishnan, D.; Crossley, A.; McEvoy, N.; Coleman, J. N.; Nicolosi, V., Liquid exfoliation of interlayer spacing-tunable 2D vanadium oxide nanosheets: High capacity and rate handling Li-ion battery cathodes. *Nano Energy* **2017,** *39*, 151-161.
8. Moretti, A.; Maroni, F.; Osada, I.; Nobili, F.; Passerini, S., V_2O_5 Aerogel as a Versatile Cathode Material for Lithium and Sodium Batteries. *ChemElectroChem* **2015,** *2* (4), 529-537.
9. Söllinger, D.; Karl, M.; Redhammer, G. J.; Schoiber, J.; Werner, V.; Zickler, G. A.; Pokrant, S., Modified $H_2V_3O_8$ to Enhance the Electrochemical Performance for Li-ion Insertion: The Influence of Prelithiation and Mo-Substitution. *ChemSusChem* **2021,** *14* (4), 1112-1121.
10. Ashton, T. E.; Hevia Borrás, D.; Iadecola, A.; Wiaderek, K. M.; Chupas, P. J.; Chapman, K. W.; Corr, S. A., Microwave-assisted synthesis and electrochemical evaluation of VO_2(B) nanostructures. *Acta Crystallographica Section B Structural Science, Crystal Engineering and Materials* **2015,** *71* (6), 722-726.
11. Petkov, V.; Trikalitis, P. N.; Bozin, E. S.; Billinge, S. J. L.; Vogt, T.; Kanatzidis, M. G., Structure of $V_2O_5{\cdot}nH_2O$ Xerogel Solved by the Atomic Pair Distribution Function Technique. *Journal of the American Chemical Society* **2002,** *124* (34), 10157-10162.
12. Sun, H.; Zhao, K., Electronic Structure and Comparative Properties of $LiNi_xMn_yCo_zO_2$ Cathode Materials. *The Journal of Physical Chemistry C* **2017,** *121* (11), 6002-6010.
13. Nitta, N.; Wu, F.; Lee, J. T.; Yushin, G., Li-ion battery materials: present and future. *Materials Today* **2015,** *18* (5), 252-264.
14. Yuan, K.; Ning, R.; Bai, M.; Hu, N.; Zhang, K.; Gu, J.; Li, Q.; Huang, Y.; Shen, C.; Xie, K., Prepotassiated V_2O_5 as the Cathode Material for High-Voltage Potassium-Ion Batteries. *Energy Technology* **2020,** *8* (1), 1900796.
15. Mukherjee, A.; Sa, N.; Phillips, P. J.; Burrell, A.; Vaughey, J.; Klie, R. F., Direct Investigation of Mg Intercalation into the Orthorhombic V_2O_5 Cathode Using Atomic-Resolution Transmission Electron Microscopy. *Chemistry of Materials* **2017,** *29* (5), 2218-2226.
16. Liu, S.; Zhu, H.; Zhang, B.; Li, G.; Zhu, H.; Ren, Y.; Geng, H.; Yang, Y.; Liu, Q.; Li, C. C., Tuning the Kinetics of Zinc-Ion Insertion/Extraction in V_2O_5 by In Situ Polyaniline

Intercalation Enables Improved Aqueous Zinc-Ion Storage Performance. *Advanced Materials* **2020,** *32* (26), 2001113.
17. Tsang, C.; Manthiram, A., Synthesis of nanocrystalline VO_2 and its electrochemical behavior in lithium batteries. *Journal of the Electrochemical Society* **1997,** *144* (2), 520.
18. Tang, H.; Xu, N.; Pei, C.; Xiong, F.; Tan, S.; Luo, W.; An, Q.; Mai, L., $H_2V_3O_8$ Nanowires as High-Capacity Cathode Materials for Magnesium-Based Battery. *ACS Applied Materials & Interfaces* **2017,** *9* (34), 28667-28673.
19. Wang, Q.; Pan, J.; Li, M.; Luo, Y.; Wu, H.; Zhong, L.; Li, G., VO_2(B) nanosheets as a cathode material for Li-ion battery. *Journal of Materials Science Technology* **2015,** *31* (6), 630-633.
20. Wang, Y.; Zhang, H. J.; Admar, A. S.; Luo, J.; Wong, C. C.; Borgna, A.; Lin, J., Improved cyclability of lithium-ion battery anode using encapsulated V_2O_3 nanostructures in well-graphitized carbon fiber. *RSC Advances* **2012,** *2* (13), 5748.
21. Xiao, B.; Zhang, B.; Tang, L.-b.; An, C.-s.; He, Z.-j.; Tong, H.; Yu, W.-j.; Zheng, J.-c., V_2O_3/rGO composite as a potential anode material for lithium ion batteries. *Ceramics International* **2018,** *44* (13), 15044-15049.
22. Shi, W.; Rui, X.; Zhu, J.; Yan, Q., Design of Nanostructured Hybrid Materials Based on Carbon and Metal Oxides for Li Ion Batteries. *The Journal of Physical Chemistry C* **2012,** *116* (51), 26685-26693.
23. Huang, X.; Qi, X.; Boey, F.; Zhang, H., Graphene-based composites. *Chem. Soc. Rev.* **2012,** *41* (2), 666-686.
~~24. Averianov, T.; Pomerantseva, E., Composite Li-ion battery cathodes formed via integration of carbon nanotubes or graphene nanoplatelets into chemical preintercalation synthesis of bilayered vanadium oxides. *Under review in the Journal of Alloys and Compounds.*~~
24. Averianov, T.; Pomerantseva, E., Composite Li-ion battery cathodes formed via integration of carbon nanotubes or graphene nanoplatelets into chemical preintercalation synthesis of bilayered vanadium oxides. *Journal of Alloys and Compounds* **2022,** 903, 163929.
25. Lei, C.; Han, F.; Li, D.; Li, W.-C.; Sun, Q.; Zhang, X.-Q.; Lu, A.-H., Dopamine as the coating agent and carbon precursor for the fabrication of N-doped carbon coated Fe_3O_4 composites as superior lithium ion anodes. *Nanoscale* **2013,** *5* (3), 1168.
26. Liu, X.; Depaifve, S.; Leyssens, T.; Hermans, S.; Vlad, A., Versatile Synthesis of Vanadium(III, IV, V) Oxides@Reduced Graphene Oxide Nanocomposites and Evaluation of their Lithium and Sodium Storage Performances. *Batteries & Supercaps* **2019,** *2* (12), 1016-1025.
27. Shi, Y.; Zhang, Z.; Wexler, D.; Chou, S.; Gao, J.; Abruña, H. D.; Li, H.; Liu, H.; Wu, Y.; Wang, J., Facile synthesis of porous V_2O_3/C composites as lithium storage material with enhanced capacity and good rate capability. *Journal of Power Sources* **2015,** *275*, 392-398.
28. Song, S.; Li, W.; Ruan, Y.; Qin, X.; Zhang, D.; Xu, Y., TiC-modified α-MnO_2 nanowires as highly efficient oxygen electrocatalyst for rechargeable Zn-air batteries. *Journal of Alloys and Compounds* **2020,** *834*, 155090.
29. Thakur, A. K.; Majumder, M.; Choudhary, R. B.; Singh, S. B., MoS_2 flakes integrated with boron and nitrogen-doped carbon: Striking gravimetric and volumetric capacitive performance for supercapacitor applications. *Journal of Power Sources* **2018,** *402*, 163-173.
30. Yoon, T.; Chae, C.; Sun, Y.-K.; Zhao, X.; Kung, H. H.; Lee, J. K., Bottom-up in situ formation of Fe_3O_4 nanocrystals in a porous carbon foam for lithium-ion battery anodes. *Journal of Materials Chemistry* **2011,** *21* (43), 17325.

31. Zhang, C.; Song, H.; Zhang, C.; Liu, C.; Liu, Y.; Cao, G., Interface Reduction Synthesis of $H_2V_3O_8$ Nanobelts–Graphene for High-Rate Li-Ion Batteries. *The Journal of Physical Chemistry C* **2015,** *119* (21), 11391-11399.
32. Liu, P.; Zhu, K.; Xu, Y.; Bian, K.; Wang, J.; Tai, G. A.; Gao, Y.; Luo, H.; Lu, L.; Liu, J., Hierarchical Porous Intercalation-Type V_2O_3 as High-Performance Anode Materials for Li-Ion Batteries. *Chemistry - A European Journal* **2017,** *23* (31), 7538-7544.
33. Zhang, Y.; Fan, M.; Zhou, M.; Huang, C.; Chen, C.; Cao, Y.; Xie, G.; Li, H.; Liu, X., Controlled synthesis and electrochemical properties of vanadium oxides with different nanostructures. *Bulletin of Materials Science* **2012,** *35* (3), 369-376.
34. Lee, H.; Dellatore, S. M.; Miller, W. M.; Messersmith, P. B., Mussel-Inspired Surface Chemistry for Multifunctional Coatings. *Science* **2007,** *318* (5849), 426-430.
35. Dong, Y.; Xu, X.; Li, S.; Han, C.; Zhao, K.; Zhang, L.; Niu, C.; Huang, Z.; Mai, L., Inhibiting effect of Na^+ pre-intercalation in MoO_3 nanobelts with enhanced electrochemical performance. *Nano Energy* **2015,** *15*, 145-152.
36. Clites, M.; Andris, R.; Cullen, D. A.; More, K. L.; Pomerantseva, E., Improving Electronic Conductivity of Layered Oxides through the Formation of Two-Dimensional Heterointerface for Intercalation Batteries. *ACS Applied Energy Materials* **2020,** *3*, 3835-3844.
~~37. Norouzi, N.; Averianov, T.; Kuang, J.; Bock, D. C.; Yan, S.; Wang, L.; Takeuchi, K. J.; Takeuchi, E. S.; Marschilok, A. C.; Pomerantseva, E., Hierarchically Structured MoO2/Dopamine-Derived Carbon Spheres as Intercalation Electrodes for Lithium-Ion Batteries. *Under review in Materials Today Chemistry*.~~
37. Norouzi, N.; Averianov, T.; Kuang, J.; Bock, D. C.; Yan, S.; Wang, L.; Takeuchi, K. J.; Takeuchi, E. S.; Marschilok, A. C.; Pomerantseva, E., Hierarchically Structured MoO_2/Dopamine-Derived Carbon Spheres as Intercalation Electrodes for Lithium-Ion Batteries. *Materials Today Chemistry* **2022,** 24, 100783.
38. Alonso, B.; Livage, J., Synthesis of Vanadium Oxide Gels from Peroxovanadic Acid Solutions: A 51V NMR Study. *Journal of Solid State Chemistry* **1999,** *148* (1), 16-19.
39. Ponzio, E. A.; Benedetti, T. M.; Torresi, R. M., Electrochemical and morphological stabilization of V_2O_5 nanofibers by the addition of polyaniline. *Electrochimica Acta* **2007,** *52* (13), 4419-4427.
40. Liu, Y. J.; Degroot, D. C.; Schindler, J. L.; Kannewurf, C. R.; Kanatzidis, M. G., Stabilization of anilinium in vanadium(V) oxide xerogel and its post-intercalative polymerization to poly(aniline) in air. **1993,** (7), 593.
41. Mallinson, D.; Mullen, A. B.; Lamprou, D. A. J. J. o. m. s., Probing polydopamine adhesion to protein and polymer films: microscopic and spectroscopic evaluation. **2018,** *53* (5), 3198-3209.
42. Qi, Y.; Chen, W.; Mai, L.; Zhu, Q.; Jin, A. J. I. J. E. S., Synthesis and electrochemical performance of PEO doped molybdenum trioxide nanobelts. **2006,** *1*, 317-323.
43. Oka, Y.; Yao, T.; Yamamoto, N., Structure determination of $H_2V_3O_8$ by powder X-ray diffraction. *Journal of Solid State Chemistry* **1990,** *89* (2), 372-377.
44. Finger, L. W.; Hazen, R. M., Crystal structure and isothermal compression of Fe_2O_3, Cr_2O_3, and V_2O_3 to 50 kbars. *Journal of Applied Physics* **1980,** *51* (10), 5362.
45. Zhang, Y.; Liu, X.; Xie, G.; Yu, L.; Yi, S.; Hu, M.; Huang, C., Hydrothermal synthesis, characterization, formation mechanism and electrochemical property of $V_3O_7{\cdot}H_2O$ single-crystal nanobelts. *Materials Science and Engineering: B* **2010,** *175* (2), 164-171.

46. Zhao, C.; Wang, X.; Kong, J.; Ang, J. M.; Lee, P. S.; Liu, Z.; Lu, X., Self-Assembly-Induced Alternately Stacked Single-Layer MoS2 and N-doped Graphene: A Novel van der Waals Heterostructure for Lithium-Ion Batteries. *ACS Applied Materials & Interfaces* **2016,** *8* (3), 2372-2379.
47. Ni, S.; Zeng, H.; Yang, X., Fabrication of VO_2(B) Nanobelts and Their Application in Lithium Ion Batteries. *Journal of Nanomaterials* **2011,** *2011*, 1-4.
48. He, P.; Quan, Y.; Xu, X.; Yan, M.; Yang, W.; An, Q.; He, L.; Mai, L., High-Performance Aqueous Zinc-Ion Battery Based on Layered $H_2V_3O_8$ Nanowire Cathode. *Small* **2017,** *13* (47), 1702551.
49. Wang, Y.; Alsmeyer, D. C.; McCreery, R. L., Raman spectroscopy of carbon materials: structural basis of observed spectra. *Chemistry of Materials* **1990,** *2* (5), 557-563.
50. Yu, X.; Fan, H.; Liu, Y.; Shi, Z.; Jin, Z., Characterization of Carbonized Polydopamine Nanoparticles Suggests Ordered Supramolecular Structure of Polydopamine. *Langmuir* **2014,** *30* (19), 5497-5505.
51. Qu, K.; Wang, J.; Ren, J.; Qu, X., Carbon Dots Prepared by Hydrothermal Treatment of Dopamine as an Effective Fluorescent Sensing Platform for the Label-Free Detection of Iron(III) Ions and Dopamine. *Chemistry - A European Journal* **2013,** *19* (22), 7243-7249.
52. Zhang, Y.; Huang, C.; Meng, C., Controlled synthesis of V_6O_{13} nanobelts by a facile one-pot hydrothermal process and their effect on thermal decomposition of ammonium perchlorate. *Materials Express* **2015,** *5* (2), 105-112.
53. Wu, C. G.; Degroot, D. C.; Marcy, H. O.; Schindler, J. L.; Kannewurf, C. R.; Liu, Y. J.; Hirpo, W.; Kanatzidis, M. G., Redox Intercalative Polymerization of Aniline in V_2O_5 Xerogel. The Postintercalative Intralamellar Polymer Growth in Polyaniline/Metal Oxide Nanocomposites Is Facilitated by Molecular Oxygen. *Chemistry of Materials* **1996,** *8* (8), 1992-2004.
54. Li, N.; Huang, W.; Shi, Q.; Zhang, Y.; Song, L., A CTAB-assisted hydrothermal synthesis of VO_2(B) nanostructures for lithium-ion battery application. *Ceramics International* **2013,** *39* (6), 6199-6206.